



HAL
open science

ROI CT reconstruction combining analytic inversion of the finite Hilbert transform and SVD

Aurélien Coussat, Simon Rit, Rolf Clackdoyle, Michel Defrise, Laurent Desbat, Jean Michel Létang

► **To cite this version:**

Aurélien Coussat, Simon Rit, Rolf Clackdoyle, Michel Defrise, Laurent Desbat, et al.. ROI CT reconstruction combining analytic inversion of the finite Hilbert transform and SVD. Sixth international conference on image formation in X-ray computed tomography, Aug 2020, Regensburg, Germany. pp.526-529. hal-03014228

HAL Id: hal-03014228

<https://hal.science/hal-03014228>

Submitted on 19 Nov 2020

HAL is a multi-disciplinary open access archive for the deposit and dissemination of scientific research documents, whether they are published or not. The documents may come from teaching and research institutions in France or abroad, or from public or private research centers.

L'archive ouverte pluridisciplinaire **HAL**, est destinée au dépôt et à la diffusion de documents scientifiques de niveau recherche, publiés ou non, émanant des établissements d'enseignement et de recherche français ou étrangers, des laboratoires publics ou privés.

ROI CT reconstruction combining analytic inversion of the finite Hilbert transform and SVD

Aurélien Coussat*, Simon Rit*, Rolf Clackdoyle†, Michel Defrise‡, Laurent Desbat†, Jean Michel Létang*

Abstract—In computed tomography, a scan of the whole object may be impossible, leading to truncated projection data. Using differentiated backprojection, the reconstruction problem can be reduced to a set of independent and one-dimensional Hilbert transforms to invert. Depending on the truncation pattern, this inversion problem can either be “zero-”, “one-” or “two-endpoint”. The zero-endpoint case is known as the interior problem: the field-of-view is completely contained in the object and the reconstruction problem has no unique solution. The two-endpoint case possesses an analytic, numerically stable inverse. The one-endpoint case has a unique and mathematically stable inverse, but no analytic formula for its inverse has been derived so far. A field-of-view (FOV) which is not interior generally contains both one- and two-endpoint sub-regions and we propose here to combine them by using the analytic two-endpoint reconstruction as additional knowledge for the one-endpoint inversion in the rest of the FOV. We hence obtain two reconstructed regions, which we chose to slightly overlap to partially correct for a small residual error appearing in the one-endpoint reconstructions.

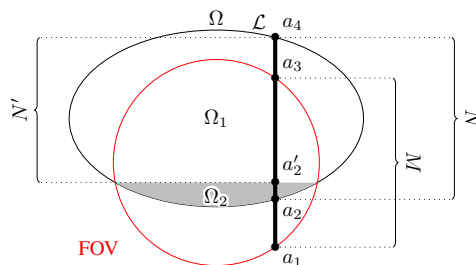


Fig. 1: Diagram summarizing our reconstruction set-up. The shape Ω is the object’s convex hull. The gray area Ω_2 is the region that can be reconstructed using the two-endpoint Hilbert inversion formula [2]. The pair (a_1, a_3) (respectively (a_2, a_4)) bounds the FOV (respectively Ω) along the segment \mathcal{L} (drawn here in the particular case where the Hilbert direction θ is equal to 0). The region Ω_1 is $\Omega \setminus \Omega_2$. We are only interested in reconstruction in $\text{FOV} \cap \Omega$.

I. INTRODUCTION

X-ray tomography conventionally requires the irradiation of an entire transaxial slice of the object to obtain an image of satisfactory quality. However, it can be undesirable or impossible to perform such an irradiation, and only a sub-region of the slice is irradiated. Conventional reconstruction approaches then become ineffective, but recent theoretical results show that accurate region-of-interest (ROI) reconstruction is possible for some patterns of projection truncation [1].

The context of this work is the two-dimensional (2D) parallel geometry, even though the results can possibly be generalized to other geometries. We assume that the convex hull of the object (denoted as Ω) is known. We define the field-of-view (FOV) of the scanner as the region where each point is irradiated over 180° . Any line segment contained in the union of the scanner FOV and Ω but whose two endpoints lie outside Ω has an analytic reconstruction formula [2] that we name the “two-endpoint Hilbert inversion”. The region inside Ω that can be reconstructed with this approach is denoted Ω_2 (Fig. 1). Line segments which have a single endpoint lying outside Ω , such as $[a_1; a_4]$ in Fig. 1, admit a unique and mathematically stable reconstruction along the part of

the line segment inside the FOV [3], although no analytic formula has yet been derived for it. Reconstruction along these segments allows reconstruction of the complete FOV for the configuration of Fig. 1. Called “one-endpoint Hilbert inversion”, this one-dimensional reconstruction problem can be solved numerically by several techniques, such as iterative methods, e.g. projection onto convex sets [3], or singular value decomposition (SVD). Our technique for one-endpoint Hilbert inversion is partially based on SVD.

A standard regularization of SVD, truncated SVD (TSVD), was extended to include support information and applied to the one-endpoint problem in a previous work [4]. Here, we push this improvement further by first applying the two-endpoint inversion formula where possible, then incorporating some knowledge about this reconstruction into the previous “extended SVD” (XSVD) inversion. Finally, the two-endpoint reconstruction is used again to estimate and partially correct for a small residual error inherent to the one-endpoint problem.

II. MATERIALS AND METHODS

Let $f : \mathbb{R}^2 \rightarrow \mathbb{R}$ be the 2D unknown function we want to recover from the measurements $p : [0; \pi] \times \mathbb{R} \rightarrow \mathbb{R}$ defined as

$$p(\phi, r) = p_\phi(r) = \int_{-\infty}^{+\infty} f(r\alpha_\phi + s\beta_\phi) ds \quad (1)$$

where $\alpha_\phi = (\cos \phi, \sin \phi)$ and $\beta_\phi = (-\sin \phi, \cos \phi)$. Here, in the context of ROI tomography, we focus on recovering f from p when the values of r span less than the extent of f , i.e., when the projections of f are truncated.

This work was partially supported by grant ANR-17-CE19-0006 (ROI doré project) from the Agence Nationale de la Recherche (France).

*Université de Lyon, INSA-Lyon, Université Claude Bernard Lyon 1, UJM-Saint Etienne, CNRS, Inserm, CREATIS UMR 5220, U1206, F-69373, Lyon, France

†Univ. Grenoble Alpes, CNRS, Grenoble INP, TIMC-IMAG, 38000 Grenoble, France

‡Department of Nuclear Medicine, Vrije Universiteit Brussel, Brussels, Belgium

The reconstruction technique introduced in this article is based on the link between the backprojection of the derivative of the measurements and the unknown function f [2]:

$$-\frac{1}{2\pi} \int_{\theta}^{\theta+\pi} \left. \frac{\partial p(\phi, r)}{\partial r} \right|_{r=\mathbf{x} \cdot \boldsymbol{\alpha}_{\phi}} d\phi = H_{\theta} f(\mathbf{x}) \quad (2)$$

where $\mathbf{x} = (x_1, x_2)$ and $H_{\theta} f$ represents the directional Hilbert transform of f in the direction of the vector $\boldsymbol{\beta}_{\theta} = (-\sin \theta, \cos \theta)$:

$$H_{\theta} f(\mathbf{x}) = \int_{-\infty}^{+\infty} \frac{f(\mathbf{x} - t\boldsymbol{\beta}_{\theta})}{\pi t} dt. \quad (3)$$

This procedure, Eq. (2), has been named differentiated backprojection (DBP), and we refer to θ as the Hilbert direction.

We assume that the samples of the DBP image are accessible at unit-spacing along each line segment \mathcal{L} , always oriented vertically in this work, as shown in Fig. 1. Along a segment \mathcal{L} , let $(a_1, a_3) \in \mathbb{N}^2$ be inner bounds of the FOV and $(a_2, a_4) \in \mathbb{N}^2$ be outer bounds of Ω with $a_1 < a_2 < a_3 < a_4$ for one-endpoint segments. Let $\mathbf{g} \in \mathbb{R}^M$ be the discretized DBP along this segment in the FOV with $M = a_3 - a_1 + 1$, and $\mathbf{f} \in \mathbb{R}^N$ the sought vector of samples of the unknown function with $N = a_4 - a_2 + 1$. By discretizing Eqs. (2) and (3), we obtain the discrete Hilbert transform operator \mathbf{H} defined as the $M \times N$ matrix with coefficients

$$H_{j-a_1+1, j'-a_2+1} = \frac{1}{\pi} \frac{1}{j - j' + \frac{1}{2}}, \quad (4)$$

$a_1 \leq j \leq a_3$ and $a_2 \leq j' \leq a_4$ such that $\mathbf{g} = \mathbf{H}\mathbf{f}$. The Hilbert transform is applied with a half-pixel shift to improve the reconstructed resolution [5].

Performing reconstruction along segment \mathcal{L} can be done by finding a pseudo-inverse $N \times M$ matrix \mathbf{H}^{\dagger} of \mathbf{H} such that $\mathbf{H}^{\dagger}\mathbf{g} = \mathbf{f}^{\dagger}$. This can be achieved by SVD: if $\mathbf{H} = \mathbf{U}\boldsymbol{\Sigma}\mathbf{V}^{\top}$ with \mathbf{U} a $M \times M$ matrix, $\boldsymbol{\Sigma}$ a $M \times N$ matrix and \mathbf{V} a $N \times N$ matrix, then $\mathbf{H}^{\dagger} = \mathbf{V}\boldsymbol{\Sigma}^{\dagger}\mathbf{U}^{\top}$ with $\boldsymbol{\Sigma}^{\dagger} \equiv 0$ except for coefficients $\Sigma_{k,k}^{\dagger} = 1/\Sigma_{k,k}$ for $k \in (1, \dots, \text{rank}(\mathbf{H}))$. In practice, this inversion is ill-conditioned, hence its regularization by TSVD: a cutoff k_c is chosen such that $0 < k_c \leq \text{rank}(\mathbf{H})$ after which the small and numerically unstable singular values $\sigma_k = \Sigma_{k,k}$ are discarded (assuming that the singular values are ranked in decreasing order). The reconstruction formula is

$$\mathbf{f}^{\text{TSVD}} = \sum_{k=1}^{k_c} c_k \mathbf{v}_k, \quad c_k = \langle \mathbf{g}, \mathbf{u}_k \rangle / \sigma_k \quad (5)$$

with \mathbf{v}_k (respectively \mathbf{u}_k) the k^{th} column of \mathbf{V} (respectively \mathbf{U}). This formula is applied to each line segment of the FOV measured in the Hilbert direction.

We previously proposed an improved TSVD reconstruction for the one-endpoint problem by incorporating p_{θ} , the measured projection information in the Hilbert direction [4]. Assume segment \mathcal{L} is at distance $r_{\mathcal{L}}$ to the origin. We define $\bar{\mathbf{f}} \in \mathbb{R}^N$ as

$$\bar{f}_i = \frac{1}{N} p(\theta, r_{\mathcal{L}}) \quad \forall i \in (1, \dots, N). \quad (6)$$

This vector corresponds to the discrete backprojection of a single ray and can be used as a rough estimation of \mathbf{f} in order

to approximate discarded singular components of Eq. (5). Equation (5) is therefore extended as follows:

$$\mathbf{f}^{\text{XSVD}} = \mathbf{f}^{\text{TSVD}} + \sum_{k=k_c+1}^N \bar{c}_k \mathbf{v}_k \quad (7)$$

with $\bar{c}_k = \langle \bar{\mathbf{f}}, \mathbf{v}_k \rangle$. We refer to Eq. (7) as XSVD standing for extended SVD. Both the TSVD and the XSVD techniques reconstruct the full-FOV. XSVD partially corrects a residual error observed with the TSVD which increases when approaching the border of the FOV due to the poorer stability of the inversion [3].

Region Ω_2 of the FOV can be analytically reconstructed by the stable two-endpoint Hilbert inversion formula [2] (using horizontal Hilbert line-segments in Fig. 1). We define $\Omega_1 = \Omega \setminus \Omega_2$. If a'_2 is the point at the intersection of segment \mathcal{L} with the boundary between Ω_1 and Ω_2 (as in Fig. 1), the segment $[a_2; a'_2[$ can be first reconstructed using two-endpoint Hilbert inversion. Denote $\mathbf{f}^{\Omega_2} \in \mathbb{R}^N$ the vector containing this reconstruction in $[1; a'_2 - a_2]$ and zeros elsewhere. Let $N' = a_4 - a'_2 + 1$ be the length of the unknown segment $[a'_2; a_4]$ and $\bar{\mathbf{f}}' \in \mathbb{R}^{N'}$ such that

$$\bar{f}'_i = \frac{1}{N'} \left(p(\theta, r_{\mathcal{L}}) - \sum_{j=1}^{a'_2-a_2} f_j^{\Omega_2} \right) \quad \forall i \in (1, \dots, N'). \quad (8)$$

The estimate $\bar{\mathbf{f}}'$ corresponds to a single backprojection of the integral sum of f in Ω_1 along \mathcal{L} . The DBP $\mathbf{g}' \in \mathbb{R}^{M'}$ of the restriction of f to Ω_1 is given by

$$\mathbf{g}' = \mathbf{g} - \mathbf{H}\mathbf{f}^{\Omega_2}. \quad (9)$$

Finally, the $M' \times N'$ matrix \mathbf{H}' , defined using a'_2 instead of a_2 , is decomposed by SVD similarly to \mathbf{H} : $\mathbf{H}' = \mathbf{U}'\boldsymbol{\Sigma}'\mathbf{V}'^{\top}$. The reconstruction using cutoff k'_c can now be defined as

$$\mathbf{f}_i^{\text{XSVD-2}} = \begin{cases} f_i^{\Omega_2} & 1 \leq i \leq N - N' \\ f_{i-(N-N')}^{\Omega_1} & N - N' + 1 \leq i \leq N \end{cases} \quad (10)$$

where

$$\mathbf{f}^{\Omega_1} = \mathbf{f}^{\text{TSVD-1}} + \sum_{k=k'_c+1}^{N'} \bar{c}'_k \mathbf{v}'_k, \quad \bar{c}'_k = \langle \bar{\mathbf{f}}', \mathbf{v}'_k \rangle \quad (11)$$

and where $\mathbf{f}^{\text{TSVD-1}} \in \mathbb{R}^{N'}$, given by

$$\mathbf{f}^{\text{TSVD-1}} = \sum_{k=1}^{k'_c} c'_k \mathbf{v}'_k, \quad c'_k = \langle \mathbf{g}', \mathbf{u}'_k \rangle / \sigma'_k. \quad (12)$$

Finally, the TSVD procedure for reconstruction in Ω is

$$\mathbf{f}_i^{\text{TSVD-2}} = \begin{cases} f_i^{\Omega_2} & 1 \leq i \leq N - N' \\ f_{i-(N-N')}^{\text{TSVD-1}} & N - N' + 1 \leq i \leq N \end{cases}. \quad (13)$$

Conceptually, these new procedures consist of “removing” the data corresponding to f^{Ω_2} from the one-endpoint problem, and reconstructing an object with support Ω_1 using Eq. (7) or (5). This reconstruction can then be combined with the two-endpoint reconstructed region Ω_2 to integrally reconstruct the full FOV.

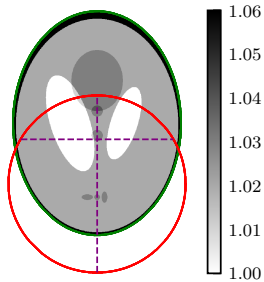


Fig. 2: Illustration of the simulation. The green oval represents the object’s convex hull Ω and the red circle the scanner’s FOV. The purple dashed lines are the profiles considered in Fig. 4.

TABLE I: Reconstructions considered in our simulations.

Reconstruction name	Two-endpoint reconstruction of Ω_2	Boundary correction	SVD extension (Eq. (7))
TSVD	No	N/A	No
TSVD-2	Yes	No	No
TSVD-2b	Yes	Yes	No
XSVD	No	N/A	Yes
XSVD-2	Yes	No	Yes
XSVD-2b	Yes	Yes	Yes

The XSVD-2 reconstruction can be further improved by enforcing continuity between the reconstructions at $a'_2 - 1$ (two-endpoint Hilbert inversion) and at a'_2 (one-endpoint Hilbert inversion). Our approach was to reconstruct $N + 1$ samples using SVD with an additional unknown sample corresponding to location $a'_2 - 1$ along \mathcal{L} and an amended definition of \mathbf{g}' , and to add the difference ϵ between two-endpoint and SVD reconstructions at $a'_2 - 1$ to the SVD reconstruction. This correction can be applied to both $\mathbf{f}^{\text{TSVD-2}}$ and $\mathbf{f}^{\text{XSVD-2}}$ and we named the new reconstructions $\mathbf{f}^{\text{TSVD-2b}}$ and $\mathbf{f}^{\text{XSVD-2b}}$.

The proposed methods were evaluated using computer simulations of the 2D Shepp-Logan phantom. A set of 720 parallel projections of 560 rays each were analytically computed over an arc of 180° . The pixel spacing of the projections and the reconstructions was approximately 0.26 mm. The set-up is illustrated in Fig. 2. The cutoffs k_c and k'_c were set to K and K' , respectively, where $K = a_3 - a_2 + 1$ and $K' = a_3 - a'_2 + 1$, as justified in a previous work [4]. Reconstructions were performed on a 1024×1024 pixel grid following various scenarios summarized in Table I. The Hilbert direction was chosen horizontal for the two-endpoint reconstruction, allowing the segment’s two endpoints to lie outside the object, and vertical for the one-endpoint, so that in both cases the Hilbert line-segments were aligned with the pixel grid.

All simulations were implemented using Python 3.7.2, NumPy 1.15.4 and RTK 2.1.0 [6].

III. RESULTS

Figure 3 shows the reconstruction results from the six scenarios of Table I. In Figs. 3a and 3d, reconstructions are entirely performed through one-endpoint Hilbert inversion (Eqs. (5) and (7)). Figures 3b and 3e show the two reconstructions without the Ω_2 to Ω_1 boundary correction at a'_2 , hence the horizontal transition artifact. In Figs. 3c and 3f, the one-endpoint reconstructions have been adjusted, enforcing vertical

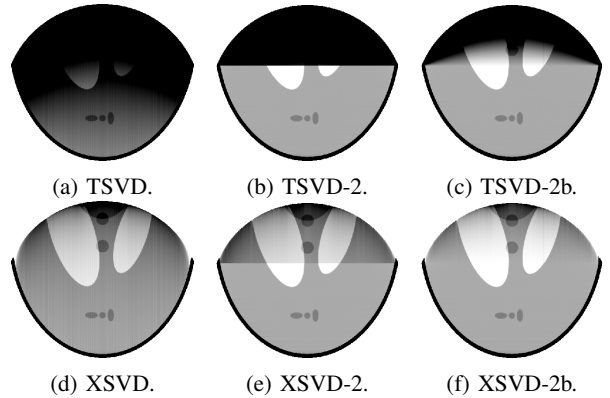


Fig. 3: Six different reconstructions of Fig. 2 from the scenarios of Table I. The grayscale is $[1; 1.06]$ as in Fig. 2.

continuity of the reconstructions. Fig. 4 shows a vertical and a horizontal profile taken in the central column and above the a'_2 threshold, respectively. In Figs. 3b, 3c, 3e and 3f, the two-endpoint reconstructions in Ω_2 are identical.

IV. DISCUSSION AND CONCLUSIONS

Figures 3a, 3d, and Fig. 4a show that in the one-endpoint setup, an offset in the reconstruction values occurs, with increasing intensity towards a_3 , the “inner” boundary of the FOV along each vertical column. The effect is smaller than appears because both Figs. 3 and 4 display only a small range of intensity values, respectively 3% and 10% of the full range of values $[0, 2]$ in the phantom. This offset feature is attributed to the rapidly decreasing stability known to occur in the one-endpoint Hilbert inversion model [3]. The fact that this same feature can be observed in other works using other approaches than SVD inversion [3], [7]–[9] suggests that the effect is intrinsic to this tomographic problem and not specific to the one-endpoint Hilbert inversion.

The main idea of the work here is to apply the stable two-endpoint method where possible, thereby reducing the load on the one-endpoint reconstructions. As expected, in the region Ω_2 where two-endpoint Hilbert inversion was applied, excellent quality reconstructions were observed; see Figs. 3b and 3e and especially Fig. 4a in the Ω_2 range $[a_2, a'_2]$. The one-endpoint method now only needs to be applied starting at a'_2 instead of a_2 , resulting in a decrease from N unknowns to N' . However, the improvement was disappointingly small there, as seen in Figs. 3b, 3e and 4.

When the two-endpoint and one-endpoint reconstructions were combined, a visible line of discontinuity appeared in the images; see Figs. 3b and 3e. Eliminating this discontinuity by adding a constant (ϵ) to the one-endpoint region $[a'_2, a_3]$ also had the benefit of reducing the offset feature, especially in the TSVD case; see Figs. 3c, 3f and 4.

To understand the disappointing outcome in the reduced region one-endpoint reconstruction, we examined the singular vectors \mathbf{u}_k and \mathbf{v}_k for the central vertical column ($x_1 = 512$) and for $k = K$ and $k = K + 1$ which are respectively the last components included, and first component excluded in series (Eq. (5)) used to build the reconstruction; see Figs. 5a and 5b.

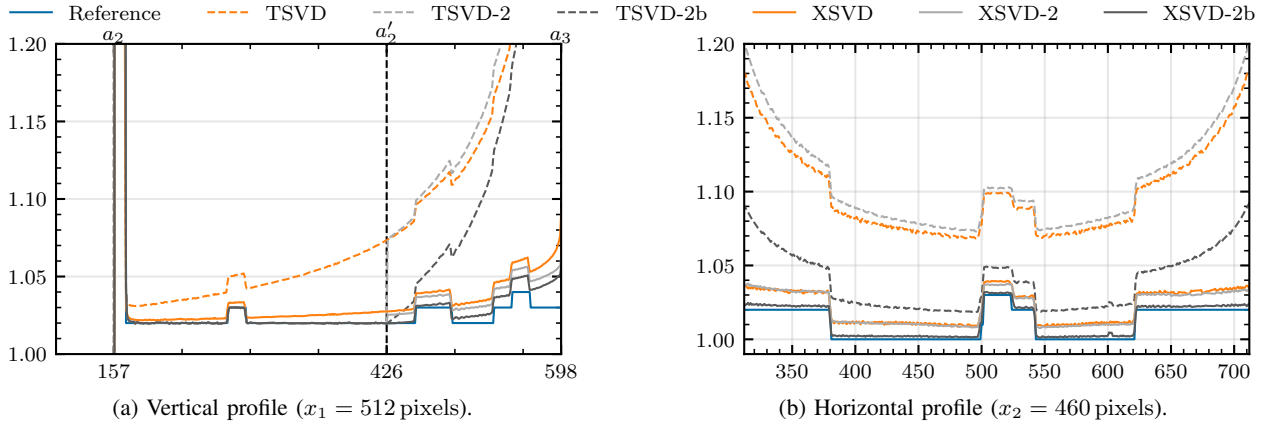


Fig. 4: Two profiles of the purple dashed lines of Fig. 2 comparing the different reconstructions described in Table I.

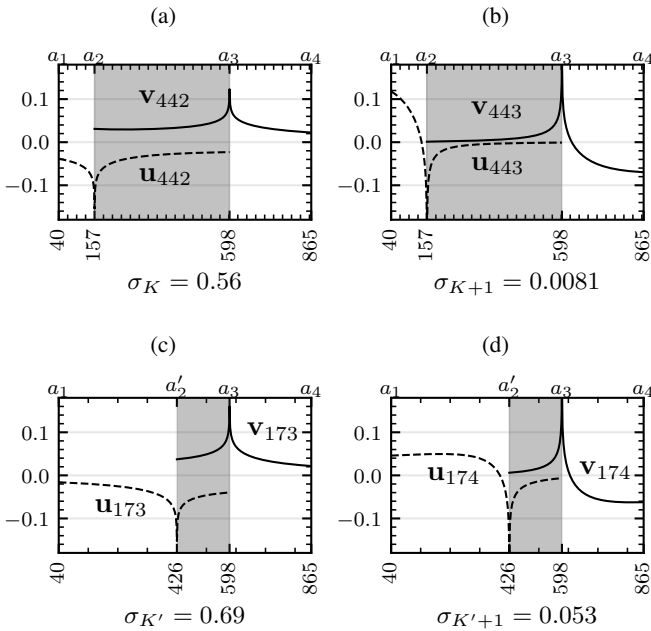


Fig. 5: Singular vectors (Eqs. (5) and (12)), mapped onto the spatial domain in the geometry of the central column of the Shepp-Logan phantom as in Fig. 2. Here, $(a_1, a_2, a'_2, a_3, a_4) = (40, 157, 426, 598, 865)$ thus $K = 442$ and $K' = 173$. (Note that K and K' are also the number of elements in the grey region.)

We concentrate on \mathbf{v}_{442} and \mathbf{v}_{443} , recalling that the desired function \mathbf{f} is expressed as the series of 709 terms with basis vectors \mathbf{v}_1 to \mathbf{v}_{709} . We noted in [4] that the lost terms from $k = 443$ to $k = 709$ corresponded to vectors \mathbf{v}_k which were very close to zero in the relevant (grey) region $[a_2, a_3]$ (inside the FOV). However, the first missing component, \mathbf{v}_{443} , when approaching a_3 inside the grey region, behaves very similarly to the offset feature in the one-endpoint reconstructions, so the absence of this term is the likely primary cause of this offset feature.

The same arguments apply for the reduced one-endpoint inversion, where the singular vectors shown in Figs. 5c and 5d are remarkably similar to those in Figs. 5a and 5b despite the

substantially different number of unknowns ($N' = 440$ instead of $N = 709$) and different SVD cutoff indices ($K' = 173$ instead of $K = 442$). Surprisingly, the horizontal stretching and shrinking of the singular vectors did not appreciably change the shape of \mathbf{v}_{174} ($K' + 1$) compared to \mathbf{v}_{443} ($K + 1$) near a_3 , which could explain the disappointingly small benefit of the reduced problem size.

In conclusion, we have proposed a method for region-of-interest reconstruction from truncated projections using Hilbert inversion methods. The two-endpoint inversion is used where possible to obtain accurate numerically stable reconstructions. The one-endpoint inversion is used elsewhere, and the characteristic offset feature has been reduced by a combination of a priori knowledge (described in [4]) and by matching reconstructed values at the boundary with the two-endpoint region. The resulting reconstructions, Fig. 3f, illustrate dramatic improvements compared to a direct TSVD approach.

REFERENCES

- [1] R. Clackdoyle and M. Defrise, "Tomographic Reconstruction in the 21st Century," *IEEE Sig. Proc. Mag.*, vol. 27, no. 4, pp. 60–80, Jul. 2010.
- [2] F. Noo, R. Clackdoyle, and J. Pack, "A two-step Hilbert transform method for 2D image reconstruction," *Phys. Med. Biol.*, vol. 49, no. 17, pp. 3903–3923, Sep. 2004.
- [3] M. Defrise, F. Noo, R. Clackdoyle, and H. Kudo, "Truncated Hilbert transform and image reconstruction from limited tomographic data," *Inverse Problems*, vol. 22, no. 3, pp. 1037–1053, Jun. 2006.
- [4] A. Coussat, S. Rit, R. Clackdoyle, M. Defrise, L. Desbat, and J. M. Létang, "Region-of-Interest CT Reconstruction using Singular Value Decomposition of the Truncated Hilbert Transform," *IEEE NSS-MIC, Manchester*, Oct. 2019.
- [5] F. Noo, J. Pack, and D. Heuscher, "Exact helical reconstruction using native cone-beam geometries," *Phys. Med. Biol.*, vol. 48, no. 23, pp. 3787–3818, Dec. 2003.
- [6] S. Rit, M. Vila Oliva, S. Brousmiche, R. Labarbe, D. Sarrut, and G. Sharp, "The Reconstruction Toolkit (RTK), an open-source cone-beam CT reconstruction toolkit based on the Insight Toolkit (ITK)," *Journal of Physics: Conference Series*, vol. 489, p. 012079, Mar. 2014.
- [7] R. Clackdoyle, F. Noo, Junyu Guo, and J. Roberts, "Quantitative reconstruction from truncated projections in classical tomography," *IEEE Trans. Nucl. Sci.*, vol. 51, no. 5, pp. 2570–2578, Oct. 2004.
- [8] E. Rashed, H. Kudo, and F. Noo, "Iterative Region-of-Interest Reconstruction From Truncated CT Projection Data Under Blind Object Support," in *IEEE NSS-MIC Conf. Rec.* IEEE, Oct. 2009, pp. 321–331.
- [9] R. Clackdoyle, F. Noo, F. Momey, L. Desbat, and S. Rit, "Accurate Transaxial Region-of-Interest Reconstruction in Helical CT?" *IEEE Trans. Rad. Plasma Med. Sci.*, vol. 1, no. 4, pp. 334–345, Jul. 2017.